



Research papers

Single-cell operando SOC and SOH diagnosis in a 24 V lithium iron phosphate battery with a voltage-controlled model

Jonas A. Braun^{a,*}, René Behmann^a, Daniel Chabrol^b, Frederik Fuchs^b, Wolfgang G. Bessler^a^a Institute of Sustainable Energy Systems (INES), Offenburg University of Applied Sciences, Badstrasse 24, 77652 Offenburg, Germany^b BENNING CMS Technology GmbH, Am Untergrün 6, 79232 March, Germany

ARTICLE INFO

Keywords:

Lithium-ion battery

State of charge (SOC)

State of health (SOH)

Battery pack

Single cell

Voltage-controlled model (VCM)

ABSTRACT

Batteries typically consist of multiple individual cells connected in series. Here we demonstrate single-cell state of charge (SOC) and state of health (SOH) diagnosis in a 24 V class lithium-ion battery. To this goal, we introduce and apply a novel, highly efficient algorithm based on a voltage-controlled model (VCM). The battery, consisting of eight single cells, is cycled over a duration of five months under a simple cycling protocol between 20 % and 100 % SOC. The cell-to-cell standard deviations obtained with the novel algorithm were 1.25 SOC-% and 1.07 SOH-% at beginning of cycling. A cell-averaged capacity loss of 9.9 % after five months cycling was observed. While the accuracy of single-cell SOC estimation was limited (probably owed to the flat voltage characteristics of the lithium iron phosphate, LFP, chemistry investigated here), single-cell SOH estimation showed a high accuracy (2.09 SOH-% mean absolute error compared to laboratory reference tests). Because the algorithm does not require observers, filters, or neural networks, it is computationally very efficient (three seconds analysis time for the complete data set consisting of eight cells with approx. 780.000 measurement points per cell).

1. Introduction

Every year around ten billion lithium-ion battery cells are being produced and assembled in batteries for a large variety of portable, mobile and stationary applications [1–3]. All those battery-powered products require a reliable diagnosis of the state of charge (SOC), which is passed as information to the user and/or is needed for energy management [4]. The SOC is usually defined [5] as the remaining dischargeable capacity Q relative to the capacity of a fully-charged battery C , mathematically expressed as

$$\text{SOC} = \frac{Q}{C} \quad (1)$$

The capacity C changes over time due to battery aging. The diagnosis of this change is highly desirable both for the user (allowing the assessment of remaining storage capability and value) and for the battery manufacturer (allowing, for example, the assessment of warranty risks or predictive maintenance strategies). The state of health (SOH) is usually defined [5] as the capacity of a fully-charged, but aged cell relative to the capacity of a fresh cell, in the following referred to as the nominal capacity C_N , as

$$\text{SOH} = \frac{C}{C_N} \quad (2)$$

Although other definitions of the SOH are possible (e.g., based on the internal resistance of the battery [6]), for the present study we use the capacity-based definition according to Eq. (2).

The measurement of SOC and/or SOH is usually referred to as state diagnosis or state estimation. It is possible with a wide variety of different methods, including Coulomb counting [7], model-based methods such as extended Kalman filters [8], and machine learning based methods [9]. Each method has advantages and disadvantages; it is beyond the scope of the present article to provide a detailed overview and discussion. The interested reader is referred to numerous books [5,6,10–12] and review articles [4,9,13–17] on the topic. For practical application, both SOC and SOH need to be estimated *in operando*, that is, during the regular operation of the battery. While laboratory tests apply “artificial” full cycles and/or well-defined constant current phases, *operando* diagnosis must typically rely on partial cycling with undefined power profiles. In practice, state diagnosis is being performed as part of the battery management system (BMS) [18], where the method of choice is implemented on a microcontroller or computer.

Battery packs usually consist of multiple, individual single cells

* Corresponding author.

E-mail address: jonas.braun@hs-offenburg.de (J.A. Braun).<https://doi.org/10.1016/j.est.2024.110986>

Received 20 November 2023; Received in revised form 24 January 2024; Accepted 15 February 2024

Available online 2 March 2024

2352-152X/© 2024 The Authors. Published by Elsevier Ltd. This is an open access article under the CC BY license (<http://creativecommons.org/licenses/by/4.0/>).

connected in series and/or in parallel [19,20]. This allows to increase voltage and/or capacity, and hence energy, to the required application level. For example, we have studied before a home storage systems consisting of large-format prismatic cells in 14s1p configuration [20]. Even larger battery packs are needed for electric vehicles (EVs). For example, the Renault Zoe (2019 edition) battery features 192 single cells in 96s2p configuration (96 serially-connected times 2 parallel-connected cells); the Tesla Model 3 (2020 edition) has 2976 cells in its battery pack [21]. All cells are expected to behave in a slightly different way, owing to both, variability in the cell production, and local thermal and electrical boundary conditions inside the pack. The differences are expected to increase during cell lifetime. Here and throughout the text we carefully distinguish between the terms *cell* (or *single cell*) and *battery* (or *pack*).

SOC and SOH diagnosis of single cells in multi-cell packs is challenging from the point of view of both, data acquisition and data analysis [18]. Concerning data acquisition, a large number of voltage, current and temperature sensors are required, and data has to be recorded with a sufficiently high time resolution (typically >1 Hz), resulting in large data sets. Concerning data analysis, the computational cost and memory requirement of filters or neural networks, even if moderate for a single cell, may easily exceed the capabilities of BMS microcontrollers when data of hundreds of individual cells need to be analyzed in real time [18,22,23]. Some authors have suggested to use a small number of “representative” cells for state diagnosis [23], reducing the computational effort. Other authors have used “mean-difference model” or “leader-follower” approaches, where two models are superimposed, a more complex one for a mean or representative cell behavior, and a simpler one for cell-to-cell differences [24–27]. Cloud-based data analysis has been demonstrated recently to circumvent limited local resources [28,29], which however significantly increases the overall implementation complexity. Hua et al. have demonstrated a multi-timescale estimation framework, where single-cell SOH is estimated only every several weeks to reduce computational load, and the analysis is used to identify a representative single cell for real-time SOC diagnosis [30].

Apart from these simplifying approaches, the published literature on true single-cell SOC and SOH diagnosis in battery packs is very sparse. Merkle et al. [28] estimated single-cell SOC and SOH in a 2014 e-Golf battery consisting of 264 cells in 88s3p configuration, using cloud-based data analysis. The data of one single charging cycle (from 13 % to 96 % SOC) was used for estimating capacity, and a 30 s dynamic cycle was used for estimating internal resistance by least-squares fitting equivalent circuit model (ECM) parameters to the measurement data. Tsai et al. used 30-min constant-current charge to estimate single-cell SOC and SOH in a three-cell pack by comparing experimental data with previously-measured charge voltage curves [31]. These methods thus relied on the presence and identification of certain characteristic operation phases. An et al. [32] estimated single-cell SOC and pack-level state of energy (SOE) in a five-cell lithium-ion battery pack operated under laboratory conditions by applying an extended Kalman filter to each cell. All three studies used lithium nickel manganese cobalt oxide (NMC) based lithium-ion batteries. Estimation of single-cell SOC only (without SOH or SOE) was shown by Park et al. in a four-cell pack using neural networks [33], by Zhang et al. in a 21-cell pack using a single-point Kalman filter [34], as well as in the context of cell balancing algorithms using Kalman filters or Coulomb counters [35,36]. All in all, the published methods strongly vary in approach and complexity.

We have recently introduced a new algorithm for SOC and SOH diagnosis of batteries using voltage-controlled models (VCM) [37]. In the present article we apply this algorithm for the first time to individual cells in a battery pack. We demonstrate single-cell *operando* SOC and SOH diagnosis over several months of operation under a simple cycling protocol. We also demonstrate for the first time the application of VCMs to lithium-ion cells using lithium iron phosphate (LiFePO₄, LFP) as positive electrode (PE) material. LFP poses particular challenges to state

diagnosis due to its flat voltage discharge behavior, a voltage hysteresis between charge and discharge, and asymmetric overpotentials [38–40]. We validate the *operando* results by comparing with laboratory single-cell characterization after pack disassembly.

2. Approach

The approach of using VCM for SOC and SOH diagnosis is schematically shown in Fig. 1. The algorithm is based on a dynamic equivalent circuit model (ECM) which is formulated such that cell voltage is the input (independent) variable and cell current is the output (dependent) variable (hence, the term voltage-controlled model) [37]. This is opposite to all common formulations used in model-based state estimation (e.g., with Kalman filters), where the ECM is formulated such that cell current is the input and cell voltage the output (current-controlled model) [4–6,8,10,13–17].

The algorithm consists of two coupled analysis steps. In the first step, shown in the upper part of Fig. 1, the dynamic model is fed with time series of the experimentally-measured voltage of a single cell, $V_{exp,cell}$. In an online application, these data would be fed continuously; in the present study, we feed the model offline with historic data. The simulation yields the SOC of the cell directly, which can be displayed to the user and/or stored for further usage. Apart from the SOC, the simulation also yields the cell current $I_{sim,cell}$ as output. The operation principle of the VCM can be understood by bringing into mind a “classical” constant voltage (CV) mode during lithium-ion battery charging. Here, as in the VCM, the cell delivers a current depending on the driving overpotential, which is the difference between the applied voltage and the open-circuit voltage. Mathematically, an ECM is represented by a differential-algebraic equation (DAE) system, which provides the relationship between the variables current I , voltage V and SOC. In a “classical” current-controlled model, I is provided as independent variable, and the DAE system is solved for V and SOC. In the present voltage-controlled model, V is provided as independent variable, and the DAE system is solved for I and SOC. The mathematical form of the ECM used here will be given and discussed below.

In the second analysis step, shown in the lower part of Fig. 1, the simulated current is used for calculating the SOH according to [37]

$$SOH_{cell} = \frac{\int_{t_0}^{t_1} |I_{exp,pack}(t)| dt}{\int_{t_0}^{t_1} |I_{sim,cell}(t)| dt} \quad (3)$$

Here, $I_{exp,pack}$ is the experimentally-measured current of the battery, which is identical for all cells due to their series connection. The integrals on the right-hand side of this equation represent two Coulomb counters for the absolute charge throughputs. The simulated charge throughput (denominator) represents the behavior of the fresh cell (the modeled cell has the nominal capacity C_N and does not age), while the experimental charge throughput (numerator) represents the behavior of the aged cell. Hence, the ratio of these values yields the SOH as defined in Eq. (2). The integration time window $t_0 \dots t_1$ used in Eq. (3) can, in principle, be set arbitrarily within the battery operation time. For the present study, we use consecutive time windows of the length of five equivalent full cycles of the cell model. This means that, starting with t_0 at beginning of test, we time-integrate both numerator and denominator

of Eq. (3) until $\int_{t_0}^{t_1} |I_{sim}(t)| dt = 10 \cdot C_N$. At this point, $SOH_{cell}(t_1)$ is calculated using Eq. (3), giving the first SOH output point. Then the two Coulomb counters are reset, and time-integration is restarted setting the new t_0 to the previous t_1 . This approach gives one SOH_{cell} value every five equivalent full cycles, corresponding to approx. 15 h under the

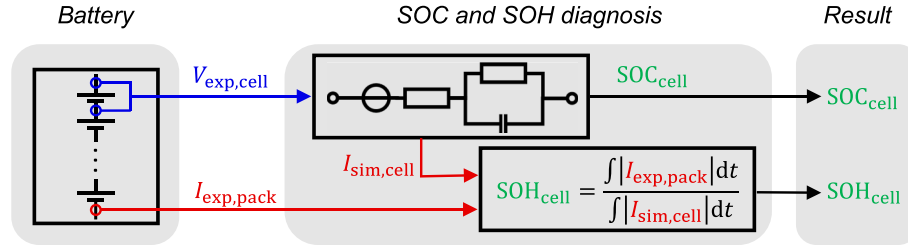


Fig. 1. Single-cell state diagnosis with a voltage-controlled model (VCM). Experimentally measured single-cell voltage $V_{exp,cell}$ is used as input for an equivalent circuit model (ECM). Model outputs are the single-cell SOC and single-cell current $I_{sim,cell}$. Simulated current and experimental current $I_{exp,pack}$ are time-integrated to obtain the absolute charge throughput. Because the model represents an unaged cell, the ratio between experimental and simulated charge throughput is the cell SOH. The algorithm is computationally efficient because it does not require filter operations, optimization procedures, or neural networks.

cycling protocol applied here. All single cells are analyzed individually; because the cells differ in their behavior, the SOH_{cell} values may be obtained at different points in time for different cells.

In summary, SOC and SOH diagnosis with VCM uses the following sequence:

1. Development and parameterization of a dynamic model that represents the behavior of the fresh (unaged) target battery. Implementation of a voltage-controlled version of the model.
2. Measurement of I_{exp} and V_{exp} as function of time during battery operation.
3. Feeding of the model with V_{exp} and simulation of I_{sim} and SOC. This gives continuous values of the estimated SOC.
4. Calculation of the integrals in Eq. (3) over a predefined time or charge throughput. Calculation of SOH with Eq. (3) when the predefined time or charge throughput it reached. This gives discrete values of the estimated SOH.

As shown before [37], this approach for SOC and SOH diagnosis has significant advantages compared to standard methods. For SOC diagnosis, only a voltage measurement is required, making the algorithm robust against well-known current measurement uncertainties causing SOC drift [7]. For SOH diagnosis, the algorithm is applicable *in operando*, that is, it does not “know” the battery operation protocol, SOC ranges, or current dynamics. Therefore, it does not require specific operation modes such as “artificial” full cycles, constant current phases, or rest phases. Neither SOC nor SOH diagnosis requires observers, filters or neural networks, therefore the algorithm is cheap in terms of computational power and memory.

The type of battery application (portable vs. stationary vs. mobile) strongly affects the dynamics of battery operation; for example, home-storage systems exhibit relatively uniform and slow battery charge/discharge, while EVs show fast battery dynamics. The approach presented here is independent of the application scenario, although the model may have to be adapted accordingly. We have demonstrated the algorithm before using single-cell laboratory experiments with lithium-ion cells operated under both, constant-current charge and discharge (where a very simple ECM consisting of only a voltage source and a resistor was shown to be sufficient) and dynamic EV load profiles (where the ECM needed to be extended with an additional dynamic resistor-capacitor element) [37].

3. Methods

3.1. Lithium-ion battery system

Experiments were carried out using a 24 V class lithium-ion battery with a nominal voltage of 25.6 V, nominal capacity of 50 Ah and nominal energy of 1.28 kWh. The battery system consisted of eight prismatic LFP battery cells (Lishen, model LP44147141) connected in 8s1p configuration. The cell voltages, battery current, and SOC_{BMS} data

were obtained from the BMS (BENNING CMS Technology η -Leveling BMS) by using its communication interface (CAN bus). An additional battery monitor (TBS Electronics e-xpert pro) was used solely for the purpose of tracking the equivalent full cycles. A grid-tied inverter (Studer Xtender XTM 2400-24) was used as charger and load.

The cycling of the battery was performed continuously with the following steps: (1) Constant current constant voltage (CCCV) charging with 50 A (1C) to 3.55 V and a cut-off current of approx. 1 A, corresponding to 100 % SOC_{BMS} ; (2) rest 20 min; (3) discharge with 1C rate until 20 % SOC_{BMS} is reached, according to the BMS; (4) rest 20 min. The capacity assumed by the BMS was adjusted to the measured capacity, therefore the absolute cycling depth (in Ah) varied during the experiment.

3.2. Reference performance tests

In order to validate the results of the operando SOH diagnosis, three reference performance tests (RPT) were performed on the single cells: one before beginning of cycling, one after 619 cycles, and one after 1314 cycles (end of cycling). For the RPTs, the battery was disassembled. The cells were tested under laboratory conditions at 25 °C ambient temperature (climate chamber Binder KB 115-S). The tests consisted of the following procedure: First, the cells were conditioned with ten 1C (50 A) constant current constant voltage (CCCV) charge-discharge cycles. Then, two CCCV charge-discharge cycles with 0.1C (5 A) and 1C (50 A) were carried out and used for the present analysis. The CC phases were stopped at the cutoff voltages of 3.55 V (charge) and 2.8 V (discharge). The CV phase was limited by a cut-off current of C/100 (0.5 A). Cycling was performed in a four-wire setup using battery cyclers with 50 A channels (BaSyTec XCTS and BaSyTec GSM). The capacity C of the cells was determined according to

$$C = \frac{C_{chg} + C_{dis}}{2}, \quad (4)$$

where, C_{chg} and C_{dis} are the measured charge and discharge capacities, respectively, of the 50 A CCCV cycle. Furthermore, internal resistance R of the cells was determined according to

$$R = \frac{\bar{V}_{chg} - \bar{V}_{dis}}{|\bar{I}_{chg}| + |\bar{I}_{dis}|}, \quad (5)$$

where, \bar{V}_{chg} and \bar{V}_{dis} are the average cell voltages during charge and discharge, respectively, \bar{I}_{chg} and \bar{I}_{dis} are the average currents during charge and discharge, respectively, and all averages were taken between 40 % and 60 % SOC.

3.3. Equivalent circuit model

The new algorithm for state diagnosis requires a model of the battery cell (cf. Fig. 1). In the present work we use an ECM because of its conceptual and computational simplicity [41], as compared to

physicochemical models [42,43] or machine learning models [44]. The ECM used in the present study is shown in Fig. 2a. It consists of an SOC-dependent voltage source $V^0(\text{SOC})$, a hysteresis voltage source η_{hys} , a series resistor R_s , and a resistor-capacitor element R_1, C_1 . From this model, the cell voltage V is given as function of current I as

$$V = V^0(\text{SOC}) + \eta_{\text{hys}}(I) - R_s \cdot I - V_{\text{RC}}(I), \quad (6)$$

where, $V^0(\text{SOC})$ is the open-circuit voltage and V_{RC} is the voltage drop over the resistor-capacitor (RC) element. The latter is given as

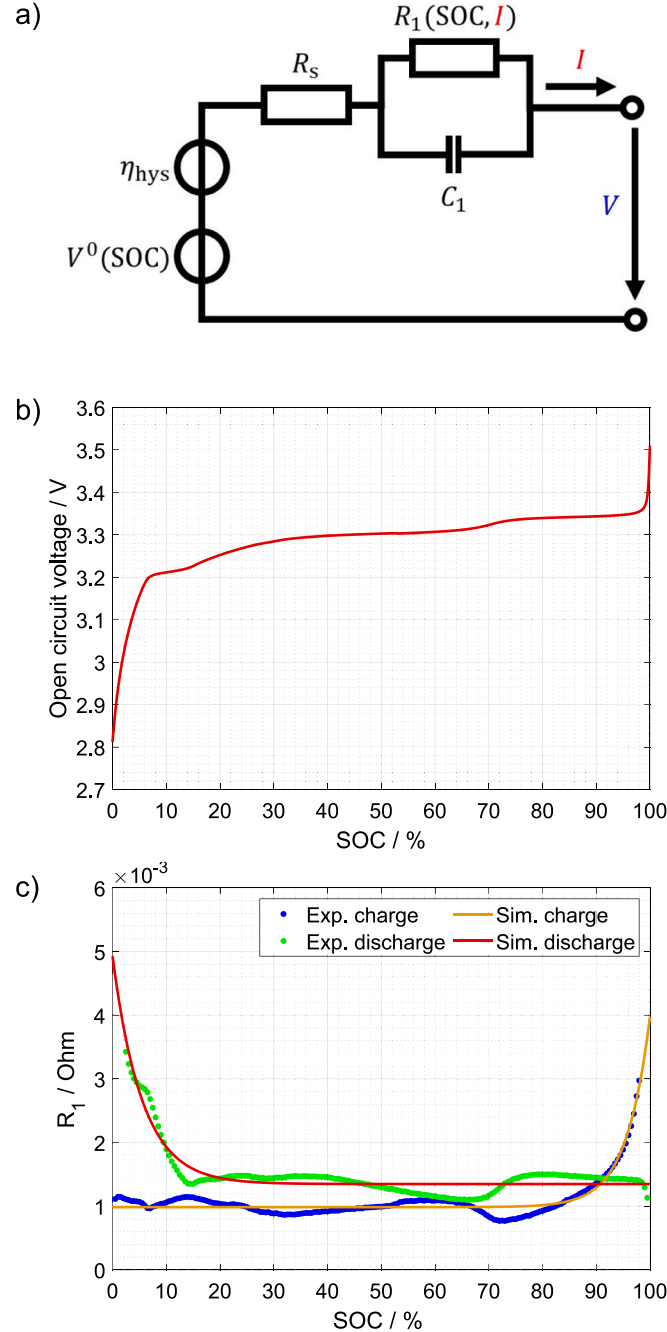


Fig. 2. Equivalent circuit model used in the present study. a The model consists of an SOC-dependent open-circuit voltage V^0 , an additional voltage source representing the OCV hysteresis η_{hys} , a serial resistor R_s , and a resistor-capacitor element R_1, C_1 ; b Pseudo-open-circuit voltage (OCV) as function of SOC, based on measurements; c resistance R_1 as function of SOC.

$$\frac{dV_{\text{RC}}}{dt} = \frac{1}{C_1} \left(I - \frac{V_{\text{RC}}}{R_1(\text{SOC}, I)} \right), \quad (7)$$

where, C_1 is the capacitance and $R_1(\text{SOC}, I)$ is the resistance which is assumed to depend on SOC and current. The SOC is given as

$$\frac{d\text{SOC}}{dt} = -\frac{I}{C_N}, \quad (8)$$

where, C_N is the nominal capacity. The combined model Eqs. (6), (7) and (8) form a DAE system. The system consists of three equations for three unknown dependent (output) variables using one independent (input) variable. In the present work, we solve this equation system either as a current-controlled model (i.e., solved for V, V_{RC} and SOC using I as input), or as voltage-controlled model (i.e., solved for I, V_{RC} and SOC using V as input). In case of a current-controlled model, Eq. (6) is explicit with respect to the output V . In case of a VCM, Eqs. (6)–(8) are implicit with respect to the output I . The inversion of the equations, that is, their solution for I at given V , is carried out numerically, as will be discussed below (Section 3.5).

3.4. Model parameterization

Dedicated laboratory experiments (in the following referred to as parameterization experiments) were carried out using an additional single cell (not part of the battery pack, but from the same delivery batch) using battery cyclers (BaSyTec XCTS, Biologic VMP3) and a climate chamber (CTS T-40/200 Li). All measurements were carried out at 25 °C. Charge and discharge curves were recorded at three different C-rates (0.05C, 0.25C, 1C) using a CCCV protocol with the same limits as in the reference performance tests (cf. section 3.2). The pseudo-OCV curve was obtained by averaging the measured $V(\text{SOC})$ curves of charge and discharge at 0.05C. The $V^0(\text{SOC})$ curve determined such is shown in Fig. 2b. In our model, we use this curve in tabular form. Alternatively, the OCV curves can also be used in the form of analytical equations [45].

Furthermore, electrochemical impedance spectroscopy (EIS) measurements were carried out at 50 % SOC. The series resistance R_s was taken as high-frequency intercept of $-Im(Z)$ in the Nyquist plot; a value of $R_s = 3.64 \cdot 10^{-4} \Omega$ was obtained. The capacitance of the RC element was obtained from the maximum of $-Im(Z)$; a value of $C_1 = 3.82 \text{ F}$ was obtained.

The internal resistance of LFP-based cells is known to asymmetrically (i.e., differently for charge and discharge) depend on SOC [40]. In order to include this effect into the model, we use two separate expressions for SOC-dependent R_1 for charge and discharge. The SOC-dependent internal resistance was obtained from the 0.05C and 1C curves as

$$R_i(\text{SOC}) = \frac{|V_{0.05C}(\text{SOC}) - V_{1C}(\text{SOC})|}{|I_{0.05C} - I_{1C}|}, \quad (9)$$

separately for charge and discharge. Based on the model structure (cf. Fig. 2a), the total internal resistance R_i is composed of

$$R_i(\text{SOC}) = R_s + R_1(\text{SOC}). \quad (10)$$

While R_s was assumed constant, the SOC dependency $R_1(\text{SOC})$ was approximated using an empirical exponential function. For the approximation, the internal resistance and previously determined series resistance were used as the data basis. The results are shown in Fig. 2c. The value for R_1 obtained such is

$$R_1(\text{SOC}, I) = \begin{cases} 3.577 \cdot 10^{-3} \Omega \cdot e^{-18.11 \cdot \text{SOC}} + 1.348 \cdot 10^{-3} \Omega & \text{for } I > 0 \text{ (discharge)} \\ 2.995 \cdot 10^{-3} \Omega \cdot e^{-22.76 \cdot (1 - \text{SOC})} + 9.848 \cdot 10^{-4} \Omega & \text{for } I < 0 \text{ (charge)} \end{cases} \quad (11)$$

The hysteresis of the OCV of LFP-based cells was determined by taking the cell voltages at 50 % SOC at 0.05C and 0.25C, linearly extrapolating towards 0C for charge and discharge voltages separately,

and taking half of the difference of the extrapolated voltages. The value obtained such is

$$\eta_{\text{hys}}(I) = \begin{cases} -24.7 \text{ mV for } I > 0 \text{ (discharge)} \\ +24.7 \text{ mV for } I < 0 \text{ (charge)} \end{cases} \quad (12)$$

For simulating the CCCV cycles of the parameterization experiments, we used the explicit form of Eqs. (11) and (12). When using the VCM for state diagnosis, these two equations are solved implicitly as part of the full equation system (see below, Section 3.5).

The nominal capacity is assumed constant at $C_N = 50 \text{ Ah}$, representing the data-sheet performance of the cell. This is consistent with the key assumption of the SOH diagnosis method used here, where the model represents a fresh cell and does not undergo aging.

3.5. Simulation methodology

For parameterization and current-controlled simulations we used a Matlab (R2019b) implementation of the ECM, using Matlab's ode23t solver to time-integrate Eqs. (6)–(8), (11) and (12). For SOC and SOH diagnosis, voltage-controlled simulations are required. In this case, Eqs. (6)–(8), (11) and (12) form an implicit equation system that needs to be solved for I , V_{RC} and SOC using V as input. Due to the nonlinear nature of the equation system, it is not possible to invert it analytically. However, it is straightforward to solve the system numerically. To this goal, the equations can be cast into the general form of a DAE system,

$$\frac{dV_{\text{RC}}}{dt} = \frac{1}{C_1} \left(I - \frac{V_{\text{RC}}}{R_1(\text{SOC}, I)} \right), \quad (13)$$

$$\frac{d\text{SOC}}{dt} = -\frac{I}{C_N}, \quad (14)$$

$$0 = V^0(\text{SOC}) + \eta_{\text{hys}}(I) - R_s I - V_{\text{RC}}(I) - V. \quad (15)$$

After inserting Eqs. (11) and (12), the right-hand sides can be implemented with standard numerical DAE solvers such as Matlab's ode23t. For the present work, we solved the DAE system in a C++ class using Euler time discretization. The resulting algorithm is very fast: Total computational time for SOC and SOH (5 months of data, 8 cells, approx. 780.000 measurement points per cell) was only 3 s on a laptop computer equipped with an Intel i7-1185G7 CPU, using a single core.

3.6. Coulomb counter

In this work, an additional Coulomb counter was used as a reference for the SOC of the battery pack. It was calculated as

$$\text{SOC}_{\text{CC}}(t) = -\frac{1}{C_N} \int_{t_0}^t I_{\text{exp}}(\tau) d\tau \quad (16)$$

with the measured current I_{exp} and the nominal capacity C_N [37]. We use the same value for the nominal capacity ($C_N = 50 \text{ Ah}$) as in the ECM. The Coulomb counter was calibrated as follows. In case one of the cells in the battery pack reached or exceeded the charge cut-off voltage (3.55 V), the SOC was set to 100 %. Similarly, the SOC was set to 0 % when one individual cell voltage reached or fell below the final discharge voltage (2.8 V).

We use a conventional Coulomb counter as reference because it is a simple and widely-used algorithm. In addition, it has a very low computational effort. There are many other, more elaborate SOC diagnosis algorithms (see literature overview in the Introduction). In future work, we plan to compare the present algorithm based on voltage-controlled models with state-of-the-art algorithms, such as Kalman filters.

3.7. Data analysis

In order to quantify the performance of the new algorithm, the following statistical values were calculated. The cell-to-cell standard deviation in estimated SOC was calculated as

$$\text{SD}_{\text{SOC}} = \frac{1}{N_{\text{points}}} \sum_{n=1}^{N_{\text{points}}} \sqrt{\frac{1}{N_{\text{cell}}} \sum_{k=1}^{N_{\text{cell}}} (\text{SOC}_{n,k} - \overline{\text{SOC}}_n)^2}, \quad (17)$$

where, the index n runs over the number of time points and the index k runs over the number of cells. The difference between SOC determined by the VCM and the Coulomb counter was calculated as

$$\text{MAD}_{\text{SOC}} = \frac{1}{N_{\text{points}}} \sum_{n=1}^{N_{\text{points}}} (|\text{SOC}_{\text{CC},n} - \overline{\text{SOC}}_n|), \quad (18)$$

where, the index CC stands for Coulomb counter. The cell-to-cell standard deviation in estimated *operando* SOH was calculated at a given point in time as

$$\text{SD}_{\text{SOH}} = \sqrt{\frac{1}{N_{\text{cell}}} \sum_{k=1}^{N_{\text{cell}}} (\text{SOH}_{n,k} - \overline{\text{SOH}}_n)^2}. \quad (19)$$

The cell-individual scatter of the *operando* SOH over consecutive points in time was calculated as standard deviation according to

$$\text{SD}_{\text{SOH,cell}} = \sqrt{\frac{1}{N_{\text{points}}} \sum_{n=1}^{N_{\text{points}}} (\text{SOH}_n - \overline{\text{SOH}})^2}. \quad (20)$$

The difference between a single-cell *operando* SOH and the average *operando* SOH over consecutive points in time was calculated as

$$D_{\text{SOH,cell}} = \left(\frac{1}{N_{\text{points}}} \sum_{n=1}^{N_{\text{points}}} \text{SOH}_n \right) - \left(\frac{1}{N_{\text{points}} N_{\text{cell}}} \sum_{n=1}^{N_{\text{points}}} \sum_{k=1}^{N_{\text{cell}}} \text{SOH}_{n,k} \right). \quad (21)$$

The standard deviation of the experimental capacities determined in the RPT is given as

$$\text{SD}_C = \sqrt{\frac{1}{N_{\text{cell}}} \sum_{k=1}^{N_{\text{cell}}} (C_k - \bar{C})^2}. \quad (22)$$

The mean absolute error (MAE) of the SOH determined *in operando* compared to the RPT is given as

$$\text{MAE}_{\text{SOH}} = \frac{1}{N_{\text{points}}} \sum_{n=1}^{N_{\text{points}}} (|\text{SOH}_{\text{RPT},n} - \text{SOH}_n|). \quad (23)$$

To quantify the quality of the parameterization, the MAE of the model output compared to parameterization data was calculated. The MAE of the voltage deviation,

$$\text{MAE}_V = \frac{1}{N_V} \sum_{m=1}^{N_V} (|V_{\text{sim},m} - V_{\text{exp},m}|), \quad (24)$$

was calculated using the simulated voltage V_{sim} and measured voltage V_{exp} . The MAE_V is calculated using charge and discharge curves at three different C-rates (cf. below, Section 4.2). The index m runs over the data points of the three charge and discharge curves.

4. Results

4.1. Battery operation

The lithium-ion battery studied here is a 24 V class 50 Ah system consisting of eight serially-connected single prismatic cells with LFP PE

and graphite negative electrode (NE) (see Section 3.1 for details). It was operated for a total of 1314 charge/discharge cycles between 100 % SOC_{BMS} and approx. 20 % SOC_{BMS}. For clarity, we use the acronym SOC_{BMS} for the SOC provided by the battery's own BMS (cf. Section 3.1). The cycling time was 66 days between July 3 and September 7, 2021 (cycles 1–619), then interrupted by an RPT of the single cells, and complemented by additional 76 days between September 15 and November 30, 2021 (cycles 620–1314). Exemplary data over a 6-h duration at beginning of test (cycles #1–3) are shown in Fig. 3. Pack current (panel a), pack voltage (panel b) and system-level SOC_{BMS} (panel c) show the behavior of the applied cycling protocol, consisting of constant-current (CC) discharge, rest phase, constant-current constant-voltage (CCCV) charge, and another rest phase. Notably, Panel d shows the individual voltages of the eight serially-connected cells. They show slight differences, indicating that even here, at beginning of life, there are cell-to-cell differences, owed probably to manufacturing differences. The single-cell voltages and the pack current will be used as input to the state diagnosis algorithm.

4.2. Model validation

For model parameterization and validation, we used an additional single cell (not included in the battery pack, but from the same delivery batch), termed reference cell in the following. Simulated charge and discharge curves at different C-rates are compared to experimental data from the reference cell in Fig. 4a. The model is able to describe the voltage characteristics with a high level of accuracy, as shown in panel b: The MAE_V (Eq. (24)) over the complete validation data (three charge and discharge curves with different C-rates) is 9.19 mV. Increasing deviations are observed towards low and, in particular, towards high

charge throughput (low SOC), owed to the nonlinearity of the voltage curves in those ranges. Notably, the capacity of the reference cell is slightly higher (50.9 Ah) compared to the battery cells (average 50.0 Ah) and the nominal capacity ($C_N = 50$ Ah). It is important to note that the model is isothermal: The model was parameterized to a cell operated at 25 °C ambient temperature, and the simulation results are independent of temperature. The consequences of this assumption will be further discussed in Section 5. For the simulations shown in Fig. 4, the model was operated under current control (i.e., given C-rate), in order to allow a direct comparison to the experiments. In the remainder of this article, following the basic principle of our diagnosis algorithm, the model will instead be solved with voltage as input and current as output.

4.3. Single-cell SOC

We first discuss results of the single-cell SOC diagnosis. The model was fed with the time series of an experimentally-measured single-cell voltage (cf. Fig. 3d), resulting in time-dependent SOC and current of that cell as simulation output. After analyzing all eight cells individually, the arithmetic average of the individual SOC_s was calculated at each point in time. In addition, the battery SOC was calculated using a standard Coulomb counter (cf. Section 3.6). The results obtained are shown in Fig. 5. Here, panel a shows six hours at beginning of the battery test (cycles 1–3), and panel b shows six hours at the end of the battery test (cycles 1312–1314). The estimated SOC_s show charge-discharge cycles between approx. 20 % and 100 % SOC. The eight individual cells show a slight cell-to-cell variation: The time-averaged standard deviation SD_{SOC} is 1.25 SOC-% and 0.908 SOC-% for the six hours shown in panels a and b, respectively (see Section 3.7 for definition of this and all other statistical values). The SOC estimated with a Coulomb counter shows a

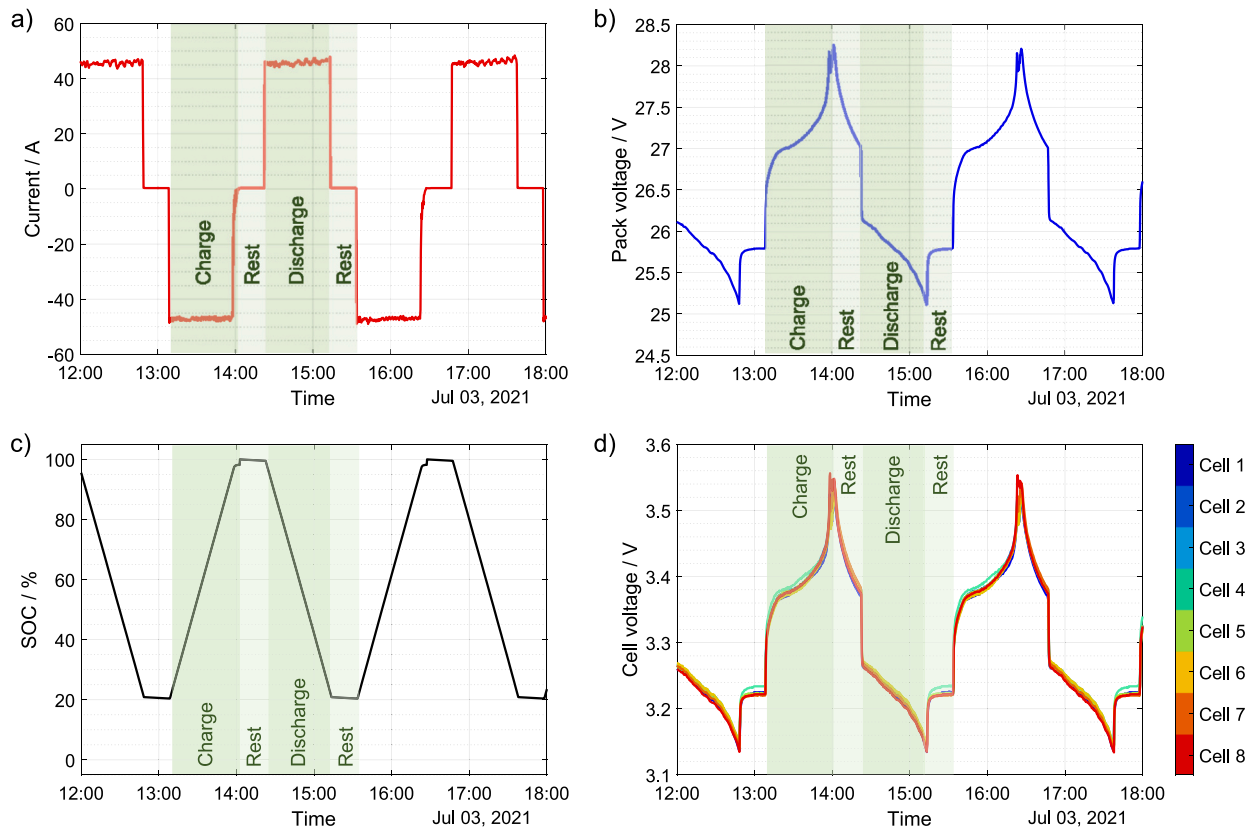


Fig. 3. Exemplary 6 h of battery operation close to beginning of cycling test. a Current within the serially-connected battery pack (50 A corresponds to nominally 1C rate; we assign positive sign of current for discharge). b Total voltage of the battery pack. c State of charge SOC_{BMS}, as provided by the battery management system. d Voltages of the eight individual cells. Small differences between the individual cells motivate the development of single-cell diagnosis. Note the flat voltage characteristics during discharge of the LFP chemistry used here.

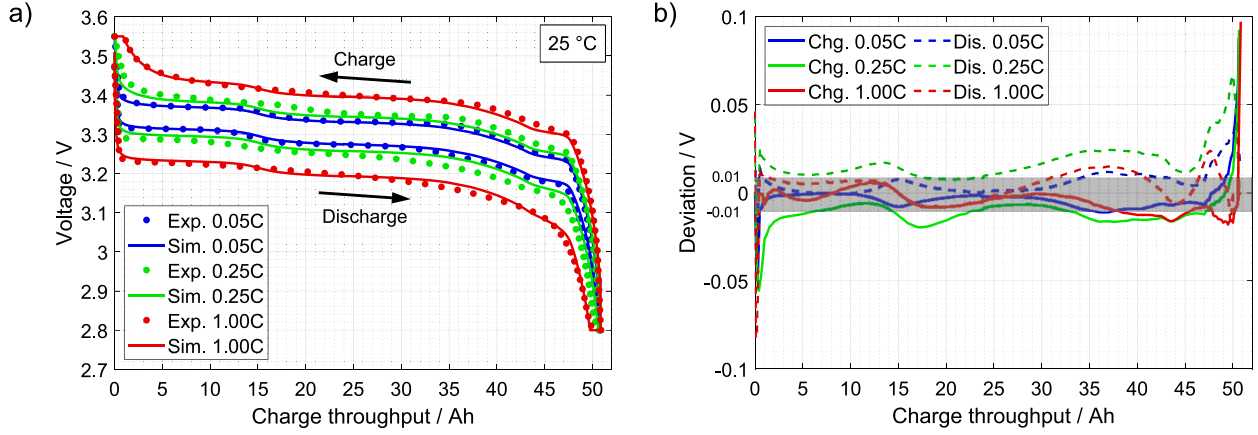


Fig. 4. Equivalent circuit model (ECM) used for the model-based state diagnosis. a Simulated charge and discharge curves using the ECM shown in Fig. 2a, in comparison to experimental data from a reference cell, at 25 °C and different C-rates. b Deviation between experiment and model, where the gray shade represents a range of ± 10 mV. The mean absolute error MAE_V (Eq. (24)) over the complete data is 9.19 mV.

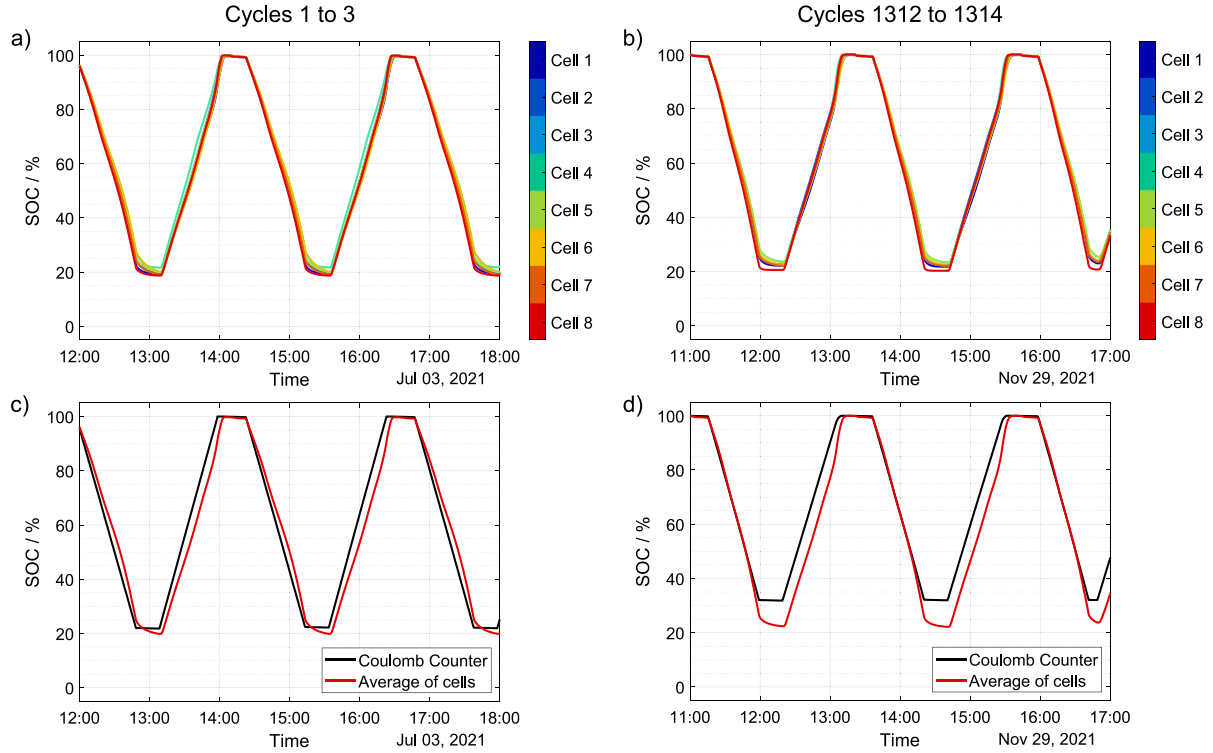


Fig. 5. Single-cell SOC during battery operation, estimated with the voltage-controlled model. a, c Exemplary 6 h at beginning of battery test. b, d Exemplary 6 h close to the end of battery test. The upper panels show the estimated single-cell SOC, the lower panels show the average SOC as well as a reference value based on a standard Coulomb counter (cf. Section 3.6).

quite linear behavior during each charge or discharge phase, resulting from the relatively constant current (cf. Fig. 3a). In contrast, the cell-averaged SOC estimated with the VCM has a slightly nonlinear behavior, which is more pronounced at the end of test. The difference between Coulomb counter and VCM is particularly apparent during the rest phase after discharge. The mean absolute difference between VCM and Coulomb counter MAD_{SOC} is 4.68 SOC-% and 4.11 SOC-% for the 6 h at beginning of test and at end of test, respectively.

4.4. Single-cell SOH

For SOH analysis, the simulated and experimental currents were evaluated for each individual cell according to Eq. (3). The results are

shown in Fig. 6. Both the single-cell SOH as well as the arithmetic average over all cells are shown. Note that, in the present work, the SOH is defined relative to the nominal capacity ($SOH_k = C_k/C_N$ with $C_N = \text{const.} = 50$ Ah, where k is cell number). The figure extends over the complete five-month operation of the battery; the data “gap” in the middle of the experiment results from the RPT after cycle #619. Clearly, the cells exhibit capacity loss, starting from 98.1 % SOH at beginning of test, and ending at 88.2 % SOH at end of test (average over all cells of first and last four SOH values). The capacity loss is nearly similar for each individual cell. The single-cell SOH data show a clear cell-to-cell difference; for the first time point, the standard deviation of the eight cells SD_{SOH} is 1.07 SOH-%. The individual single-cell SOHs also show a significant point-to-point scatter. A quantitative analysis is given in

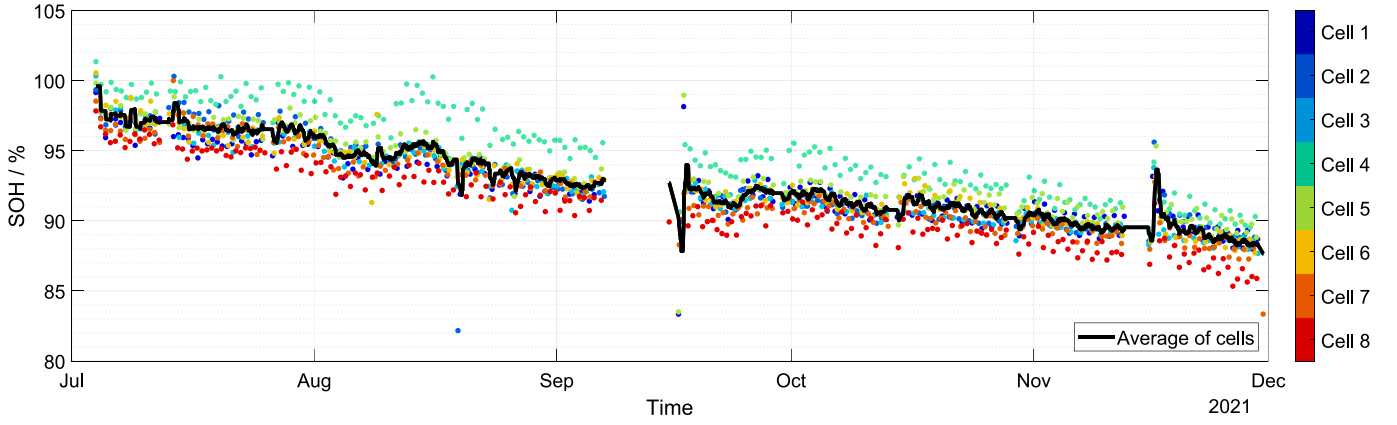


Fig. 6. Single-cell operando SOH during battery operation, estimated with the voltage-controlled model. Each point represents results of the analysis of one single cell during one time interval (five equivalent full cycles, cf. Eq. (3) and text for details). The black solid line represents the average of the eight single cells. We define the SOH of cell k as $\text{SOH}_k = C_k/C_N$ (cf. Eq. (2)); this means that all values are given relative to the nominal capacity (here: $C_N = 50$ Ah) which is identical for all cells. The range of SOH values, at each given point in time, therefore represents the range of estimated single-cell capacities. The data show a gap in September due to the RPT carried out there. Cell-to-cell variation is 1.07 SOH-% (standard deviation) at beginning of cycling, and the cells show an average capacity loss of 9.9 % during the operation time.

Table 1

Analysis of scatter (standard deviation, $\text{SD}_{\text{SOH,cell}}$) and difference to the average value ($\text{D}_{\text{SOH,cell}}$) of the SOH for a representative period from Jul 16 to Jul 26, 2021, consisting of 14 data points per cell. The average SOH in this period over all points and all cells is 96.5 %.

Cell number	$\text{SD}_{\text{SOH,cell}}$ of each cell / SOH-%	Difference D_{SOH} to average / SOH-%
1	0.427	-1.01
2	0.597	0.707
3	0.553	-0.338
4	0.780	2.34
5	0.654	0.283
6	0.417	-0.318
7	0.640	-0.181
8	0.197	-1.48

Table 1 for a representative 10-day period. The cells show an average point-to-point scatter of around 0.533 SOH-%; this number is representative of the precision of the new algorithm. The cell-individual differences to the average SOH are in the range of ≤ 1 SOH-%, with two outlier cells (#4 and #8). These findings will be further discussed in Section 5.

4.5. Reference performance tests

In order to assess the accuracy of the SOH diagnosis shown above, RPTs of the individual single cells were carried out under controlled laboratory conditions before start of battery test, after 619 cycles, and after 1314 cycles. For this purpose, the battery was disassembled, the cells characterized, and the battery reassembled after RPT. Results are shown in Fig. 7. Panels a and b show charge/discharge curves at 0.1C and 1C rate, respectively, of the single cells before operation of the battery. The cells exhibit the typical behavior of LFP/graphite chemistries [40]: At 0.1C (panel a) the voltage curve shows extended plateaus and characteristic voltage steps owed to the graphite NE; at 1C (panel b), the behavior is asymmetric with respect to charge and discharge (the branches do not run in parallel towards high and low SOC), owed to the LFP PE. Comparing the set of curves, it becomes clear that the individual cells exhibit a different behavior in terms of both, absolute voltages and the position of the voltage steps: they differ in capacity and in internal resistance. Panels c and d show RPT results after 1314 cycles of battery operation. The behavior remains qualitatively unchanged, although the capacity of the cells has clearly decreased. For further comparison, we

have quantified the capacity and the internal resistance of the individual cells from the three RPTs. Capacities are shown in panel e. Before the test, the cells have an average capacity of 50.0 Ah, corresponding exactly to the nominal data-sheet capacity of 50 Ah, with a standard deviation SD_C of 0.224 Ah. After 619 and 1314 cycles in the battery, average capacity has decreased to 46.8 Ah and 45.2 Ah, respectively: the cells clearly exhibit aging. The cell-to-cell scatter has slightly increased at 1314 cycles. Internal resistances are shown in panel f. The cell-to-cell scatter in resistance is significantly higher than the scatter in capacity; also, there is no clear trend when comparing the average values (2.02, 1.95 and 1.92 m Ω) upon progressing cycling (fresh cells, 619 cycles, 1314 cycles, respectively).

4.6. SOH validation

A direct comparison of the results of the single-cell operando SOH (Fig. 6) and the SOH determined in the RPTs (Fig. 7) is shown in Fig. 8. Each data point corresponds to one single cell at a specific point in time. The RPT SOH before the test are compared to the average first four data points of the operando SOH; the RPT SOH during the test break is compared to the average operando SOH of the two data points before and after the break; and the RPT SOH after test is compared to the average last four data points of the operando SOH. Fig. 8 plots operando SOH as function of RPT SOH, such that an exact agreement would yield points along a line through the origin, as indicated in the figure.

The results show that the new operando SOH diagnosis is in good agreement with the RPT and is able to quantitatively capture the aging trend. The MAE_{SOH} (deviation of operando SOH to RPT SOH) over all data points is 2.09 SOH-%. The data points show some scatter which is increasing with increasing cycling time (MAE_{SOH} over all cells for the three RPTs are 1.95, 1.89 and 2.42 SOH-% at beginning, middle, and end of test, respectively). Overall, these numbers demonstrate a good accuracy of the new algorithm. When taking the average over all cells, the agreement further improves slightly (MAE_{SOH} of the three cell-averaged data points is only 1.95 SOH-%). Furthermore, two cells show a comparatively high but opposite deviation, namely cells #4 and cells #8. For these two “outlier” cells, operando SOH and RPT SOH exhibit an opposite behavior at end of test (cell #4 is the “best” cell in the operando diagnosis and the “worst” cell in the RPT; cell #8 shows the opposite behavior). Potential reasons include a difference in internal resistance or open-circuit voltage curve of these cells, compared to the reference cell used for model parameterization; this will be further discussed in Section 5.

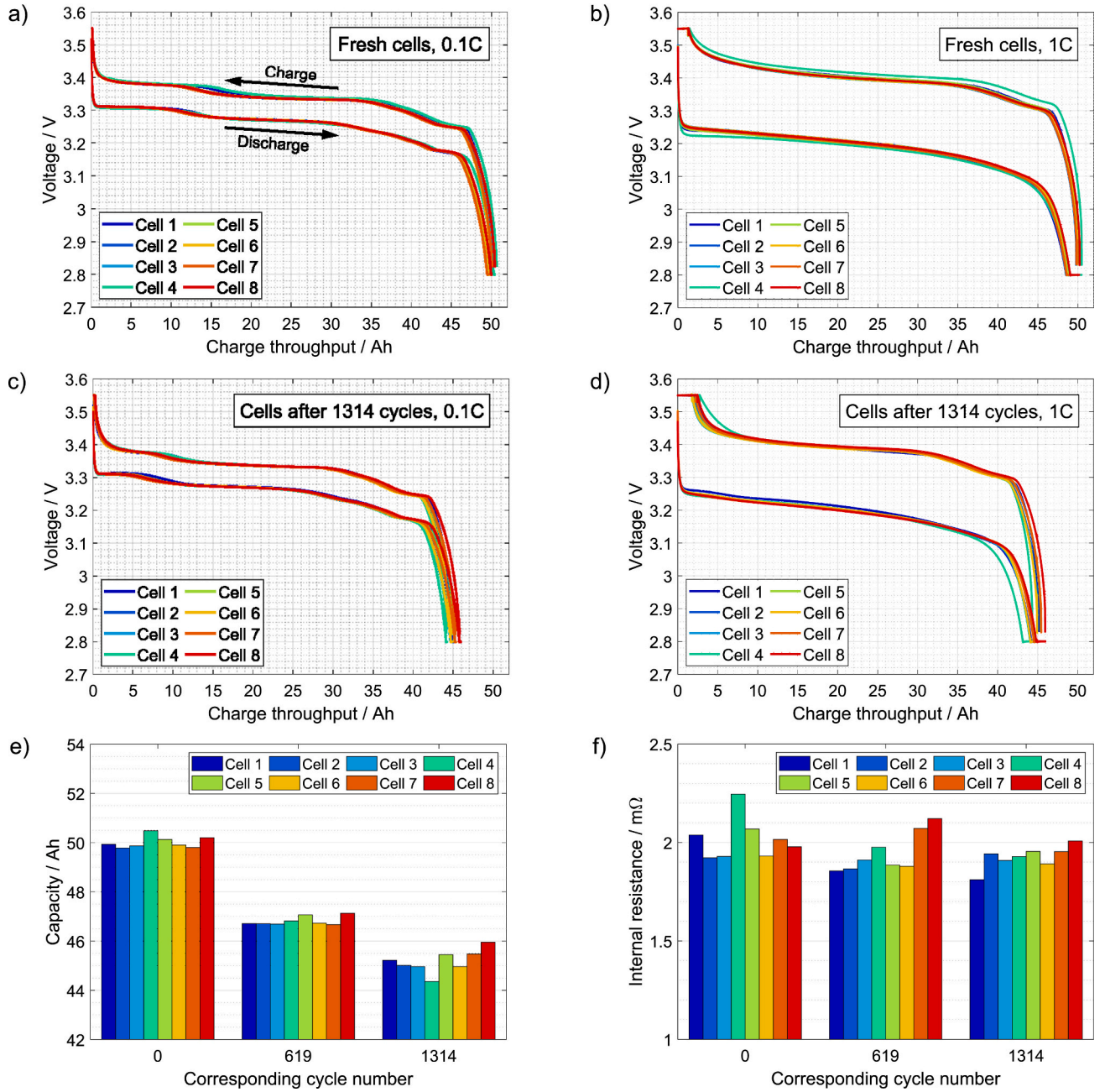


Fig. 7. Results of laboratory reference performance tests. a, b Fresh cells: charge/discharge curves at 0.1C rate and at 1C rate. c, d Cells after 1314 cycles of the battery: charge/discharge curves at 0.1C rate and at 1C rate. e Capacities of all cells before test, after 619 cycles, and after 1314 cycles, obtained from the 1C tests. f Internal resistances of all cells, obtained from the 1C tests.

5. Discussion and outlook

The results shown in the previous section represent, to the best of our knowledge, the first single-cell operando SOH diagnosis within an LFP battery pack shown in literature. Still, the accuracy of the SOC and SOH estimates demonstrated here is limited ($MAD_{SOC} = 4.68$ SOC-% compared to a Coulomb counter, $MAE_{SOH} = 2.09$ SOH-% compared to RPTs). It should be repeated that the LFP chemistry used in the present study is particularly challenging for state diagnosis because of the flat discharge voltage characteristics, charge/discharge hysteresis of the open-circuit voltage, and asymmetric overpotentials [38–40]. Indeed, the lower SOC limit of approx. 20 % used in the present cycling protocol is right within the battery's voltage plateau. In a VCM, flat voltage curves result in an increased uncertainty in the estimated SOC.

Because the algorithm is based on a model, the accuracy of both SOC and SOH diagnosis can be improved by further improving the model fidelity. To this goal, we suggest two main pathways for future work. Firstly, the model used here is isothermal. However, cell temperatures are expected to vary both on a short time scale of minutes to hours (cells are known to exhibit a significant temperature variation during cycling [40]) and on a long time scale of weeks to months (e.g., due to seasonal variations of the ambient temperature or due to cell aging that changes the thermal signature). For example, during the RPTs, an increase of cell surface temperature of up to 7 K above the ambient temperature was observed for 1C cycles. In future studies, using measured cell temperature as additional input to a model where the key parameters (in particular, R_s and R_1) are thermally activated is expected to improve both accuracy and precision of the diagnostic algorithm.

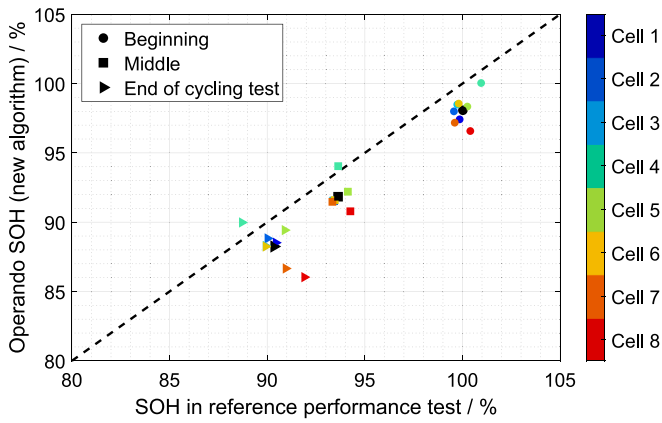


Fig. 8. Comparison of the operando single-cell SOH (new algorithm) with the SOH obtained in the reference performance tests. Each data point corresponds to one single cell at one of three points in time (beginning, middle, and end of cycling test). The dashed line is a guide to the eye, it corresponds to exact agreement between the two data sets. The average values, shown as black symbols, show a good accuracy (MAE_{SOH} of 1.95 SOH-%), as do the single-cell values (MAE_{SOH} over all data points of 2.09 SOH-%) of the new algorithm, compared to the RPT. Note that we define the SOH relative to the nominal capacity (here: $C_N = 50$ Ah) which is identical for all cells.

Secondly, the model uses parameters that are identical for all single cells and do not change with consecutive cell aging (i.e., the parameters $V^0(SOC)$, C_N , R_s , R_1 and C_1 are cell-invariant and time-invariant). This reduces the model fidelity upon progressive aging, likely causing the decreased accuracy and precision of SOC and SOH estimates observed here for the aged battery pack. The estimation accuracy of the two “outlier” cells (cf. Section 4.6) could likely be improved by using cell-individual parameters. Future studies should therefore focus on model parameter adaptation (both in terms of progressive aging and individual cells).

A limitation of the present study is the fact that the battery pack was operated in a continuous 1C cycling protocol between 20 % and 100 % SOC. Although this information does not enter the algorithm, its applicability to arbitrary battery load profiles (including dynamic load profiles that are typical for EVs), as has been demonstrated before on the cell level [37], has yet to be shown and will be subject of ongoing studies.

6. Summary and conclusions

In the present work we have demonstrated *operando* SOC and SOH diagnosis of the eight single cells of a 24 V class lithium-ion battery pack. To this goal, we have applied a new algorithm based on a voltage-controlled model (VCM) [37]. The algorithm uses measured single-cell voltage as input to an ECM, resulting in simulated single-cell SOC and current as output. By comparing the simulated current with the measured battery current, the SOH is determined.

State diagnosis with VCMs does not require observers, filters or neural networks. For SOC diagnosis, the model used here requires numerical time-solution of a differential-algebraic equation system consisting of only three unknown states (SOC, I , V_{RC}). For SOH diagnosis, only two additional Coulomb counters are required, processing the simulated and the experimental currents. The algorithm is therefore significantly simpler (both conceptually and computationally) than other diagnosis algorithms. In the present work we have used a C++ implementation of the algorithm. The total computational time (5 months of data, 8 cells, approx. 780.000 measurement points per cell) was only 3 s on a laptop computer. Although not shown in the present work, the implementation on a microcontroller should be straightforward.

For the battery studied here, single-cell SOC diagnosis was carried out successfully over the complete five-months cycling time. The cells were shown to operate in consecutive cycles between approx. 20 % and 100 % SOC. The observed cell-to-cell scatter had a standard deviation SD_{SOC} of 1.25 SOC-% at beginning of test. It is notable that SOC diagnosis was possible in the aged battery pack without requiring adaptive model parameters. However, a significant difference between cell-averaged SOC and a reference Coulomb counter ($MAD_{SOC} = 4.68$ SOC-% at beginning of test) was observed. This difference is likely a result of the flat discharge voltage characteristics of the cells' LFP chemistry.

Single-cell *operando* SOH diagnosis was also demonstrated successfully over the complete battery cycling time. The algorithm yields one SOH data point every five equivalent full cycles (around every 15 h under the present cycling protocol). At beginning of test, the cell-to-cell scatter (standard deviation SD_{SOH}) was 1.07 SOH-%. The cells were shown to exhibit an average of 9.9 % capacity loss over the five-month duration of the experiment. The precision of the algorithm (point-to-point scatter of a single cell $SD_{SOH,cell}$) was around 0.533 SOH-%. A comparison of the *operando* results with laboratory RPTs shows a good accuracy of the algorithm ($MAE_{SOH} = 2.09$ SOH-% over the complete experiment).

To the best of our knowledge, this work is the first time that SOC and SOH diagnosis with VCMs was applied to single cells of a battery pack. It is also the first time that *operando* single-cell SOH diagnosis was applied to a battery with LFP-based cells. These results underline that the new algorithm is a promising approach towards battery state diagnosis.

CRedit authorship contribution statement

Jonas A. Braun: Writing – review & editing, Visualization, Software, Methodology, Investigation, Formal analysis. **René Behmann:** Writing – review & editing, Investigation. **Daniel Chabrol:** Writing – review & editing, Investigation. **Frederik Fuchs:** Writing – review & editing, Supervision, Project administration, Methodology. **Wolfgang G. Bessler:** Writing – original draft, Supervision, Project administration, Methodology, Funding acquisition, Conceptualization.

Declaration of competing interest

The algorithms used in the present study are subject to intellectual property rights, including, but not necessarily limited to, German patent DE102019127828B4 and international patent application WO2021073690A2. Author WB is inventor of the algorithms. Authors DC and FF are affiliated to the company that owns the above-mentioned patents. All authors declare that they have no other known competing financial interests or personal relationships that could have appeared to influence the work reported in this paper.

Data availability

Data will be made available on request.

Acknowledgements

This work was funded by the German Research Foundation (DFG) in the framework of the research training group SiMET – Simulation mechano-electro-thermal processes in lithium-ion batteries (281041241/GRK 2218). R.B. acknowledges funding from the German State of Baden-Württemberg as part of the *Mittelbauprogramm 2019* program. Experiments were carried out in the Enerlab 4.0 laboratory, which was funded by the German Federal Ministry of Education and Research (BMBF) under grant no. 13FH0911N6. The authors thank David Schmdier (Offenburg University of Applied Sciences) for supporting experimental data analysis.

References

- [1] M. Armand, J.-M. Tarascon, Building better batteries, *Nature* 451 (652–657) (2008), <https://doi.org/10.1038/451652a>.
- [2] B. Nykvist, M. Nilsson, Rapidly falling costs of battery packs for electric vehicles, *Nat. Clim. Chang.* 5 (329–332) (2015), <https://doi.org/10.1038/NCLIMATE2564>.
- [3] M.S. Ziegler, J.E. Trancik, Re-examining rates of lithium-ion battery technology improvement and cost decline, *Energy Environ. Sci.* 14 (1635–1651) (2021), <https://doi.org/10.1039/D0EE02681F>.
- [4] S. Park, et al., Review of state-of-the-art battery state estimation technologies for battery management systems of stationary energy storage systems, *J. Power Electron.* 20 (2020) 1526–1540, <https://doi.org/10.1007/s43236-020-00122-7>.
- [5] V. Pop, H.J. Bergveld, D. Danilov, P.P.L. Regtien, P. Notten, *Battery Management Systems. Accurate State-of-Charge Indication for Battery-Powered Applications*, Springer, 2008.
- [6] A. Fotouhi, K. Propp, D.J. Auger, S. Longo, State of charge and state of health estimation over the battery lifespan, in: G. Pistoia, B. Liaw (Eds.), *Behaviour of Lithium-Ion Batteries in Electric Vehicles* vol. 96, Springer International Publishing, Cham, 2018, pp. 267–288.
- [7] K. Movassagh, A. Raihan, B. Balasingam, K. Pattipati, A critical look at coulomb counting approach for state of charge estimation in batteries, *Energies* 14 (4074) (2021), <https://doi.org/10.3390/en144074>.
- [8] G.L. Plett, Extended Kalman filtering for battery management systems of LiPB-based HEV battery packs, *J. Power Sources* 134 (252–261) (2004), <https://doi.org/10.1016/j.jpowsour.2004.02.031>.
- [9] Z. Ren, C. Du, A review of machine learning state-of-charge and state-of-health estimation algorithms for lithium-ion batteries, *Energy Rep.* 9 (2993–3021) (2023), <https://doi.org/10.1016/j.egyr.2023.01.108>.
- [10] R. Xiong, *Battery Management Algorithm for Electric Vehicles*, Springer, China Machine Press, Singapore, 2020.
- [11] C.D. Rahn, C.-Y. Wang, *Battery Systems Engineering*, Wiley, Chichester, UK, 2013.
- [12] G.L. Plett, *Battery Management Systems* vol. 2: Equivalent-circuit Methods (Artech House, Boston, London), 2016.
- [13] W. Waag, C. Fleischer, D.U. Sauer, Critical review of the methods for monitoring of lithium-ion batteries in electric and hybrid vehicles, *J. Power Sources* 258 (321–339) (2014), <https://doi.org/10.1016/j.jpowsour.2014.02.064>.
- [14] M. Bercibar, et al., Critical review of state of health estimation methods of Li-ion batteries for real applications, *Renew. Sust. Energ. Rev.* 56 (572–587) (2016), <https://doi.org/10.1016/j.rser.2015.11.042>.
- [15] Z. Li, J. Huang, B.Y. Liaw, J. Zhang, On state-of-charge determination for lithium-ion batteries, *J. Power Sources* 348 (281–301) (2017), <https://doi.org/10.1016/j.jpowsour.2017.03.001>.
- [16] M.A. Hannan, M. Lipu, A. Hussain, A. Mohamed, A review of lithium-ion battery state of charge estimation and management system in electric vehicle applications: challenges and recommendations, *Renew. Sust. Energ. Rev.* 78 (834–854) (2017), <https://doi.org/10.1016/j.rser.2017.05.001>.
- [17] L. Lu, X. Han, J. Li, J. Hua, M. Ouyang, A review on the key issues for lithium-ion battery management in electric vehicles, *J. Power Sources* 226 (272–288) (2013), <https://doi.org/10.1016/j.jpowsour.2012.10.060>.
- [18] M. Naguib, P. Kollmeyer, A. Emadi, Lithium-ion battery pack robust state of charge estimation, cell inconsistency, and balancing: review, *IEEE Access* 9 (50570–50582) (2021), <https://doi.org/10.1109/ACCESS.2021.3068776>.
- [19] U. Koehler, *Lithium-ion battery system design*, in: R. Korthauer (Ed.), *Lithium-Ion Batteries: Basics and Applications*, Springer, Berlin Heidelberg, Berlin, Heidelberg, 2018, pp. 89–100.
- [20] M.C. Yagci, T. Feldmann, E. Bollin, M. Schmidt, W.G. Bessler, Aging characteristics of stationary lithium-ion battery systems with serial and parallel cell configurations, *Energies* 15 (3922) (2022), <https://doi.org/10.3390/en15113922>.
- [21] L. Lander, et al., Breaking it down: a techno-economic assessment of the impact of battery pack design on disassembly costs, *Appl. Energy* 331 (2023) 120437, <https://doi.org/10.1016/j.apenergy.2022.120437>.
- [22] F. Naseri, et al., Digital twin of electric vehicle battery systems: comprehensive review of the use cases, requirements, and platforms, *Renew. Sust. Energ. Rev.* 179 (2023) 113280, <https://doi.org/10.1016/j.rser.2023.113280>.
- [23] F. An, W. Zhang, B. Sun, J. Jiang, X. Fan, A novel state-of-energy simplified estimation method for lithium-ion battery pack based on prediction and representative cells, *J. Energy Storage* 63 (2023) 107083, <https://doi.org/10.1016/j.est.2023.107083>.
- [24] F. Liu, D. Yu, W. Su, F. Bu, Multi-state joint estimation of series battery pack based on multi-model fusion, *Electrochim. Acta* 443 (2023) 141964, <https://doi.org/10.1016/j.electacta.2023.141964>.
- [25] X. Tang, Y. Zhou, F. Gao, X. Lai, Joint estimation of state-of-charge and state-of-health for all cells in the battery pack using “leader-follower” strategy, *eTransportation* 15 (2023) 100213, <https://doi.org/10.1016/j.etrans.2022.100213>.
- [26] H. Dai, X. Wei, Z. Sun, J. Wang, W. Gu, Online cell SOC estimation of Li-ion battery packs using a dual time-scale Kalman filtering for EV applications, *Appl. Energy* 95 (227–237) (2012), <https://doi.org/10.1016/j.apenergy.2012.02.044>.
- [27] S. Zhang, N. Peng, H. Lu, R. Li, X. Zhang, A systematic and low-complexity multi-state estimation framework for series-connected lithium-ion battery pack under passive balance control, *J. Energy Storage* 48 (2022) 103989, <https://doi.org/10.1016/j.est.2022.103989>.
- [28] L. Merkle, M. Pöthig, F. Schmid, Estimate e-golf battery state using diagnostic data and a digital twin, *Batteries* 7 (15) (2021), <https://doi.org/10.3390/batteries7010015>.
- [29] W. Li, et al., Digital twin for battery systems: cloud battery management system with online state-of-charge and state-of-health estimation, *J. Energy Storage* 30 (2020) 101557, <https://doi.org/10.1016/j.est.2020.101557>.
- [30] Y. Hua, A. Cordoba-Arenas, N. Warner, G. Rizzoni, A multi time-scale state-of-charge and state-of-health estimation framework using nonlinear predictive filter for lithium-ion battery pack with passive balance control, *J. Power Sources* 280 (293–312) (2015), <https://doi.org/10.1016/j.jpowsour.2015.01.112>.
- [31] M.-R. Tsai, K.-C. Chen, One single polynomial function-based charge voltage curve and its application to estimate the states of lithium-ion batteries in series, *J. Energy Storage* 59 (2023) 106502, <https://doi.org/10.1016/j.est.2022.106502>.
- [32] F. An, J. Jiang, W. Zhang, C. Zhang, X. Fan, State of energy estimation for Lithium-ion battery pack via prediction in electric vehicle applications, *IEEE Trans. Veh. Technol.* 71 (184–195) (2022), <https://doi.org/10.1109/TVT.2021.3125194>.
- [33] J. Park, J. Lee, S. Kim, I. Lee, Real-time state of charge estimation for each cell of Lithium battery pack using neural networks, *Appl. Sci.* 10 (8644) (2020), <https://doi.org/10.3390/app10238644>.
- [34] Zhang, F. et al. State-of-charge estimation based on microcontroller-implemented sigma-point Kalman filter in a modular cell balancing system for Lithium-ion battery packs. In 2015 IEEE 16th Workshop on Control and Modeling for Power Electronics (COMPEL) (IEEE72015), pp. 1–7.
- [35] C.N. Van, Optimal control of active cell balancing for Lithium-ion battery pack with constraints on cells’ current and temperature, *J. Electrochem. Energy Convers. Storage* 20 (2023), <https://doi.org/10.1115/1.4054530>.
- [36] E. J., et al., Effects analysis on active equalization control of lithium-ion batteries based on intelligent estimation of the state-of-charge, *Energy* 238 (2022) 121822, <https://doi.org/10.1016/j.energy.2021.121822>.
- [37] J.A. Braun, R. Behmann, D. Schmider, W.G. Bessler, State of charge and state of health diagnosis of batteries with voltage-controlled models, *J. Power Sources* 544 (2022) 231828, <https://doi.org/10.1016/j.jpowsour.2022.231828>.
- [38] W. Dreyer, et al., The thermodynamic origin of hysteresis in insertion batteries, *Nat. Mater.* 9 (448–453) (2010), <https://doi.org/10.1038/nmat2730>.
- [39] J. Lim, et al., Origin and hysteresis of lithium compositional spatio-dynamics within battery primary particles, *Science (New York, N.Y.)* 353 (6216) 566–571, <https://doi.org/10.1126/science.aaf4914>.
- [40] M.C. Yagci, et al., Electrical and structural characterization of large-format lithium iron phosphate cells used in home-storage systems, *Energ. Technol.* 9 (2000911) (2021), <https://doi.org/10.1002/ente.202000911>.
- [41] S. Nejad, D.T. Gladwin, D.A. Stone, A systematic review of lumped-parameter equivalent circuit models for real-time estimation of lithium-ion battery states, *J. Power Sources* 316 (183–196) (2016), <https://doi.org/10.1016/j.jpowsour.2016.03.042>.
- [42] A. Seaman, T.-S. Dao, J. McPhee, A survey of mathematics-based equivalent-circuit and electrochemical battery models for hybrid and electric vehicle simulation, *J. Power Sources* 256 (410–423) (2014), <https://doi.org/10.1016/j.jpowsour.2014.01.057>.
- [43] S. Carelli, W.G. Bessler, Coupling Lithium plating with SEI formation in a Pseudo-3D model: a comprehensive approach to describe aging in Lithium-ion cells, *J. Electrochem. Soc.* 169 (2022) 50539, <https://doi.org/10.1149/1945-7111/ac716a>.
- [44] J. Brucker, R. Behmann, W.G. Bessler, R. Gaspar, Neural ordinary differential equations for Grey-Box Modelling of lithium-ion batteries on the basis of an equivalent circuit model, *Energies* 15 (2661) (2022), <https://doi.org/10.3390/en15072661>.
- [45] S. Santhanagopalan, Q. Guo, P. Ramadass, R.E. White, Review of models for predicting the cycling performance of lithium ion batteries, *J. Power Sources* 156 (620–628) (2006), <https://doi.org/10.1016/j.jpowsour.2005.05.070>.